Dynamics of Hole Singlet-Triplet Qubits with Large g-Factor Differences

Daniel Jirovec,[1,*] Philipp M. Mutter,[2,†] Andrea Hofmann,[1,3] Alessandro Crippa,[1,4] Marek Rychetsky,[5] David L. Craig,[5] Josip Kukucka,[1] Frederico Martins,[1,6] Andrea Ballabio,[7] Natalia Ares,[8] Daniel Chrastina,[7] Giovanni Isella,[7] Guido Burkard,[2] and Georgios Katsaros[1]

[1]*Institute of Science and Technology Austria (ISTA), Am Campus 1, 3400 Klosterneuburg, Austria*
[2]*Department of Physics, University of Konstanz, D-78457 Konstanz, Germany*
[3]*Department of Physics, University of Basel, Klingelbergstrasse 82, CH-4056 Basel, Switzerland*
[4]*NEST, Istituto Nanoscienze-CNR and Scuola Normale Superiore, I-56127 Pisa, Italy*
[5]*Department of Materials, University of Oxford, Parks Road, Oxford OX1 3PH, United Kingdom*
[6]*Hitachi Cambridge Laboratory, J.J. Thomson Avenue, Cambridge CB3 0HE, United Kingdom*
[7]*L-NESS, Physics Department, Politecnico di Milano, via Anzani 42, 22100, Como, Italy*
[8]*Department of Engineering Science, University of Oxford, Parks Road, Oxford OX1 3PJ, United Kingdom*

(Received 6 October 2021; revised 24 January 2022; accepted 24 February 2022; published 24 March 2022)

The spin-orbit interaction permits to control the state of a spin qubit via electric fields. For holes it is particularly strong, allowing for fast all electrical qubit manipulation, and yet an in-depth understanding of this interaction in hole systems is missing. Here we investigate, experimentally and theoretically, the effect of the cubic Rashba spin-orbit interaction on the mixing of the spin states by studying singlet-triplet oscillations in a planar Ge hole double quantum dot. Landau-Zener sweeps at different magnetic field directions allow us to disentangle the effects of the spin-orbit induced spin-flip term from those caused by strongly site-dependent and anisotropic quantum dot g tensors. Our work, therefore, provides new insights into the hole spin-orbit interaction, necessary for optimizing future qubit experiments.

DOI: 10.1103/PhysRevLett.128.126803

The spin-orbit interaction (SOI) allows electrical manipulation of individual spins and has therefore become a key ingredient for the realization of fully electrically controlled spin qubits [1,2]. For electrons in Si it is rather weak and synthetically boosted by means of micromagnets [3,4]. For holes, on the other hand, it is an intrinsic property which allows to perform electron dipole spin resonance (EDSR) measurements [1,2,5–9]. In Ge it is particularly strong leading to Rabi frequencies beyond 100 MHz [7,10,11]. SOI for holes can be linear or cubic in the wave vector k, with nanowire qubits favoring the former type while planar qubits the latter [12–14]. The SOI is not only important for single spin but also for singlet-triplet qubits as it causes an intrinsic mixing between the heavy hole (HH) and light hole (LH) bands and thereby locally affects the g factors of the individual spins allowing to drive $S - T_0$ oscillations [15]. In combination with an extrinsic Rashba type SOI caused by the structural inversion asymmetry induced by the heterostructure, it also mixes the S and T_- states contributing therefore to a measurable avoided crossing Δ_{ST_-}.

Here, we investigate this avoided crossing for a double quantum dot (DQD) Ge hole spin system and gain insight into the interplay between SOI and the g-factor anisotropy and their consequences on qubit dynamics.

A scanning electron microscope (SEM) image of the device under consideration is depicted in Fig. 1(a) and further details can be found in Ref. [15]. A two-dimensional hole gas is embedded in a Ge/SiGe heterostructure and additional TiPd top gates confine a DQD and a charge sensor (CS). For qubit state selective read out we rely on Pauli spin blockade (PSB) combined with Ohmic reflectometry [16]. Fast detuning pulses are applied to gates LB and RB through an arbitrary waveform generator (AWG) with a pulse-rise time of $\tau_{\text{rise}} \approx 2$ ns. Throughout this work we apply a small magnetic field in a plane perpendicular to the axis connecting the two dots (DQD axis), $\mathbf{B} = [B\cos(\theta), 0, B\sin(\theta)]$, where θ describes the tilt angle from the in-plane direction. We tune the DQD to a charge transition between an effective $(2,0) \leftrightarrow (1,1)$ state, with (n_L, n_R), where n_L (n_R) denotes the effective hole number in the left (right) QD [Fig. 1(c)]. The tunnel coupling between the dots is described by t_C while the energy detuning between the $S(2,0)$ and $S(1,1)$ state is parametrized by ϵ. Each QD is characterized by an out-of-plane and an in-plane g factor, $g_\perp$ and $g_\parallel$, respectively. However, the dynamics of singlet-triplet qubits is only

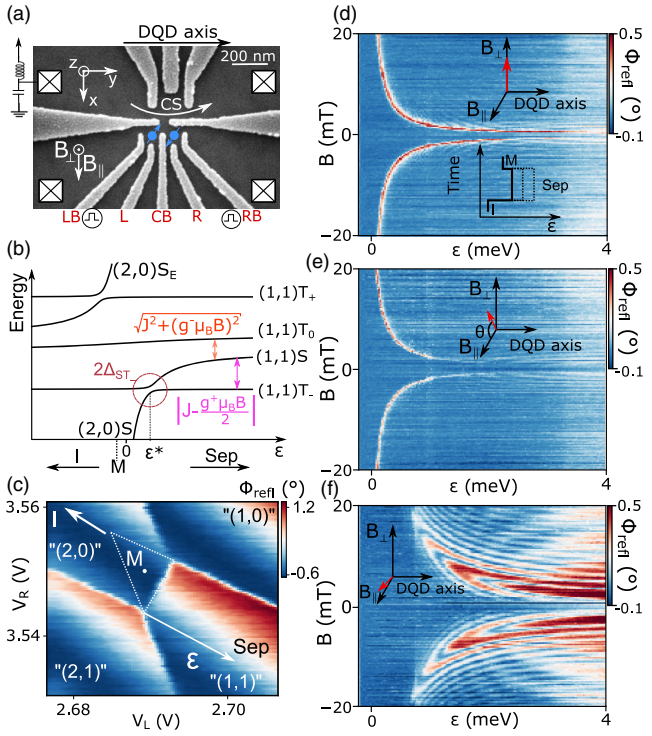

FIG. 1. (a) SEM image of the device. (b) The energy level diagram as a function of detuning highlights the relevant energy splittings between S and T_0 (orange) and S and T_- (pink). At $\epsilon = \epsilon^*$, S and T_- anticross with a splitting $2\Delta_{ST_-}$. Initialization (I) in a singlet $S(2,0)$ occurs at negative ϵ. The spins are separated (Sep) at positive ϵ. Spin-selective read out happens at the measurement point (M, white dot). (c) Stability diagram of the transition of interest. The effective hole number is reported as "(n_L, n_R)." The detuning axis as well as I, M, and Sep are highlighted. The dashed triangle marks the PSB region. (d)–(f) Reflection phase versus ϵ and magnetic field for $\theta = 90°$, 60°, and 10°, respectively. A high signal corresponds to a larger triplet return probability. The lower inset in (d) displays the pulse sequence where only the pulse amplitude ϵ is varied.

sensitive to differences in, or the average of, the Zeeman energies of the dots, and hence we define $g^{\pm} = g^L \pm g^R$ as the g-factor difference and sum. The energy spectrum of the system (the complete Hamiltonian H_{tot} is derived in the Supplemental Material [17] Sec. VI) is depicted in Fig. 1(b) as a function of ϵ. At $\epsilon = \epsilon^*$ the S and T_- states anticross.

We start by mapping out Δ_{ST_-} as a function of magnetic field angle by varying the magnetic field strength B and ϵ [24]. We initialize the system deep in (2,0) in a singlet state [point I in Fig. 1(c)], then pulse quickly to (1,1) where the spins are separated (Sep). Mixing between S and T_- is induced when $\epsilon \approx \epsilon^*$. In the end we measure the spin state inside the PSB triangle (M). The resulting triplet return probability depends both on the size of the avoided crossing and the separation time τ_S. We apply a rapid pulse of duration $\tau_S = 65$ ns and varying ϵ [inset of Fig. 1(d)]. Figures 1(d),1(e), and 1(f) depict the phase response of the charge sensor in the measurement point as a function of ϵ and B for $\theta = 90°$, 60°, and 10°, respectively. A high phase signal corresponds to a larger triplet return probability. In the out-of-plane direction we observe the expected funnel shape of the $S - T_-$ anticrossing [24]. At 60° we similarly observe a typical funnel shape, however, we notice the line to be fainter, which indicates a smaller Δ_{ST_-}. The picture drastically changes towards the in-plane direction where the $S - T_-$ avoided crossing develops interference fringes with a pattern resembling a butterfly; 2 components can be attributed to $S - T_-$ oscillations at low detuning and $S - T_0$ oscillations becoming more prominent at high detuning. The angular anisotropy of the funnel pattern, further exemplified in the Supplemental Material [17], Fig. S5, is the main focus of this work and requires knowledge of the full Hamiltonian and therefore an understanding of the interplay between the g-factor anisotropy and the spin-flip element t_{SO}.

In order to extract the g-factor anisotropy we rely on singlet-triplet oscillations. After initialization in $S(2,0)$, appropriate pulses to (1,1) induce either $S - T_0$ or $S - T_-$ oscillations. The probability to maintain the initial eigenstate of the system after a sweep with ramp time τ_R is given by the Landau-Zener formula $P_{\text{LZ}} = \exp[-(2\pi\Delta^2_{ST_-}/\hbar v)]$ [25,26], where $\hbar$ is the reduced Planck constant, $v = |dE/dt| = |dJ(\epsilon)/d\epsilon|_{\epsilon=\epsilon^*}(\Delta\epsilon/\tau_R)$ is the velocity calculated at $\epsilon = \epsilon^*$ and $J(\epsilon) = \sqrt{(\epsilon^2/4) + 2t_C^2} - (\epsilon/2)$ is the exchange energy [Fig. 1(b)] [15]. If v satisfies the diabatic condition ($P_{\text{LZ}} \approx 1$) $S - T_0$ oscillations with a frequency $f = (1/h)\sqrt{J^2 + (g^- \mu_B B)^2}$ will be favored. With $P_{\text{LZ}} < 1$ the $S - T_0$ oscillations are suppressed and the qubit is initialized in a superposition of S and T_-. After a time τ_S the system is pulsed back to the measurement point where another nondiabatic passage will cause an interference between the two states [27]. The accumulated phase difference is then given by $\phi = 2\pi f_{S-T_-}\tau_S \approx (\tau_S/\hbar)|J - \frac{1}{2}g^+\mu_B B|$ [28] [Fig. 1(b)]. As the oscillation frequency of the $S - T_0$ ($S - T_-$) qubit depends on g^- (g^+) [Fig. 1(b)] we can extract the individual g factors without the need for EDSR. We fix the magnetic field at $|B| = 2$ mT and observe the oscillations vs τ_S while rotating B. We use a fast pulse ($\tau_R = \tau_{\text{rise}} = 2$ ns) in Fig. 2(a) and a ramped pulse with ramp time $\tau_R = 100$ ns in Fig. 2(c). In both cases we pulse to $\epsilon = 4$ meV for a duration τ_S. From the fast Fourier transform (FFT) in Figs. 2(b) and 2(d) we extract the oscillation frequency f_{S-T_0} (orange dots) and f_{S-T_-} (pink dots). We notice that for $\theta \in [-25°, +25°]$ in both FFT plots the $S - T_-$ frequency is visible, suggesting that a large coupling term inducing $S - T_-$ oscillations is present at these magnetic field directions, in line with the observations in Fig. 1(f). Moreover, in Fig. 2(d) the FFT power vanishes for $\theta \approx 60°$ indicating that the ramp time τ_R induces a completely diabatic passage over the avoided crossing. This is in line with Fig. 1(e) where we observed a

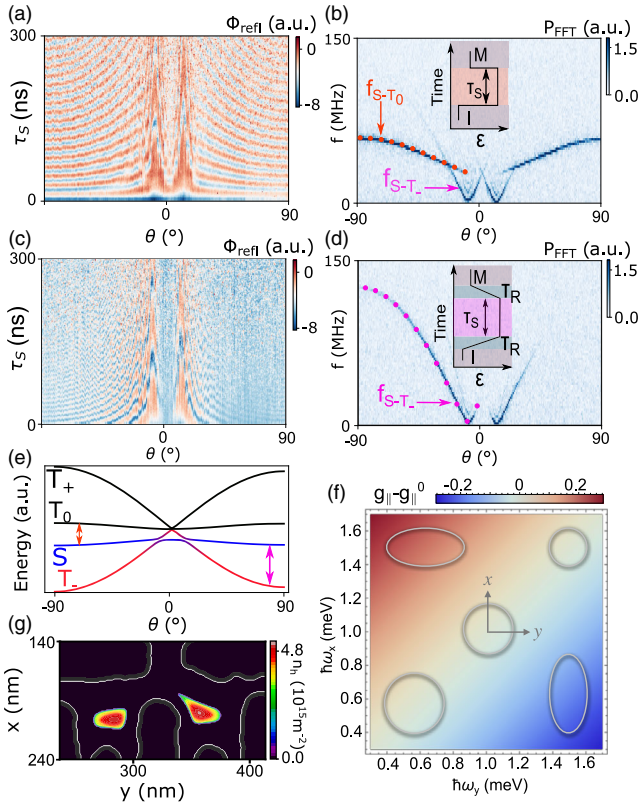

FIG. 2. (a) and (c) Oscillation amplitude of the singlet state in the measurement point as a function of separation time and magnetic field angle at $B = 2$ mT for $\tau_R = 2$ and $\tau_R = 100$ ns, respectively. (b) and (d) FFT of (a) and (c) revealing the oscillation frequency anisotropy. The orange and pink dotted lines are fit to our model. We find a small offset of 100 μT in the perpendicular field which leads to a small asymmetry in the FFT plots. The insets show the pulse shape where the system is swept to $\epsilon = 4$ meV. (e) The energy dispersion of the eigenstates of H_{tot} at $\epsilon = 4$ meV as a function of θ reproduce the frequencies seen in (b),(d) with the orange (pink) arrow highlighting the visible transition. (f) Effect of the confinement on the in-plane g factors for a quantum well width of 20 nm according to Eq. (1). On top, we schematically show possible dot geometries in real space. (g) DQD potential obtained with an electrostatic simulation analogous to that presented in Ref. [29]. Using the gate voltages from the experiment we can infer the approximate dot shapes which shows an almost opposite elongation for the two QDs. The color scale represents the hole density (n_h).

sharper $S - T_-$ avoided-crossing characteristic of a smaller mixing term.

The lines arising in the FFT plots can be fit by the energy splitting between the three lowest lying states of the system depicted in Fig. 2(e) with $g_\perp^+ = 12.00$, $g_\perp^- = 2.04$, $g_\parallel^+ = 0.10$, $g_\parallel^- = 0.43$, and $t_C = 11.38$ μeV. The latter is extracted from exchange oscillation measurements (see Supplemental Material [17] Fig. S2).

Interestingly $|g_\parallel^-| > |g_\parallel^+|$ while $|g_\perp^-| < |g_\perp^+|$. This means that the g factors in the out-of-plane direction have the same sign while they exhibit opposite signs in the in-plane direction. To understand this observation we investigate the effect of the dot geometry on the g factors. As is shown in Supplemental Material [17] Sec. VIII by using the semimicroscopic Luttinger-Kohn Hamiltonian as a starting point, the effects of the intrinsic HH-LH mixing and an elliptical confinement potential can combine to yield g-factor renormalizations. While the correction to the out-of-plane g factor is $|\delta g_\perp| < 10^{-2}$ for the values considered and hence negligible, the in-plane g factor can be altered considerably,

$$g_\parallel = g_\parallel^0 - \xi_1 \frac{\hbar(\omega_x - \omega_y)}{\hbar(\omega_x + \omega_y) - \xi_2 \Delta}. \tag{1}$$

Here, $\xi_1 \approx 20.3$ and $\xi_2 \approx 6.0$ are material specific constants, Δ is the HH-LH splitting, $\hbar\omega_{x,y}$ are the in-plane confinement energies, and $g_\parallel^0 = 0.2$ for Ge [30]. It can be seen from Fig. 2(f) that the in-plane g-factor corrections can be negative in one dot but not in the other for opposite elliptical confinement.

Electrostatic simulations of the DQD potentials arising from the applied gate voltages [29], not accounting for random disorder potentials, confirm the differently shaped dots. In fact, both dots appear elongated with the major axis of the dots being almost perpendicular to each other [Fig. 2(g) shows the calculated hole density n_h and Supplemental Material [17] Sec. IX gives details about the simulation].

We now turn to extract t_{SO} by analyzing Δ_{ST_-} in more detail. We perform Landau-Zener sweeps at $|B| = 20$ mT and extract Δ_{ST_-} from P_{LZ} [Fig. 3(b)] and repeat this for different θ. We vary τ_R during the first passage over the avoided crossing, creating a superposition of S and T_-, and keep the return sweep diabatic in order to maintain this superposition [Fig. 3(a) and inset of Fig. 3(b)]. The extracted Δ_{ST_-} is reported for different θ in Fig. 3(c). In general, Δ_{ST_-} may depend on effects influencing the hole spins such as the g-factor differences in the two dots, the SOI and possible effective magnetic field gradients caused by the hyperfine interaction [31]. While the hyperfine interaction can result in a strong out-of-plane hyperfine component δb_Z for HH states due to a special Ising-type form [32], the inhomogeneous dephasing times extracted for $B_\perp$ of $\approx$700 ns at 1 mT in Ref. [15] give an upper limit for the hyperfine component $\delta b_Z < 2$ neV, suggesting that the effects of the nuclear spin bath may safely be neglected.

In planar HH DQD systems the SOI can be parametrized by a real in-plane spin-orbit vector $\mathbf{t}_{\mathrm{SO}} = (t_x, t_y, 0)$. Such in-plane spin-flip tunneling terms stem from the cubic Rashba SOI [33], while this type of SOI does not induce out-of-plane terms t_z. In a basis in which the total Hamiltonian is diagonal in the absence of the SOI and g-factor differences, the $S - T_-$ splitting has the form [34]

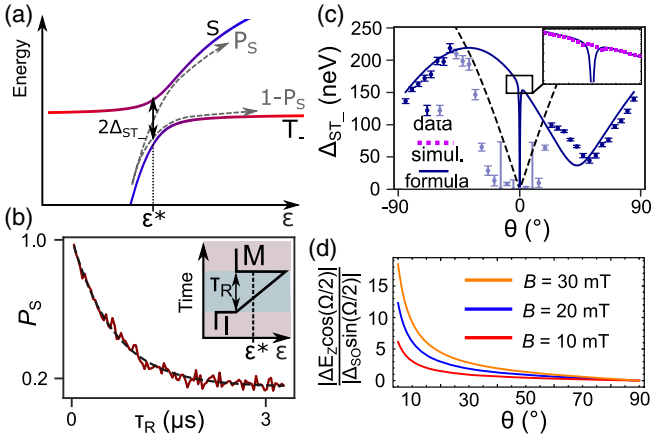

FIG. 3. (a) Energy level diagram of the states involved in the passage over the avoided crossing [red circle in 1(b)]. The probability P_S to maintain a singlet after a single passage over the avoided crossing is given by the Landau-Zener formula. (b) The single LZ passage pulse sequence (inset) leads to a singlet return probability P_S that decays exponentially with the ramp time τ_R. A fit to the Landau-Zener transition formula (black dashed line) allows to extract Δ_{ST_-}. (c) Δ_{ST_-} as a function of magnetic field angle. The extracted Δ_{ST_-} is fit to Eq. (2) with t_x and t_y as fitting parameters (solid blue line). The black dashed line represents the maximum Δ_{ST_-} as a function of θ that can be reliably measured by a single LZ passage. The light colored data points are, therefore, excluded from the fit. (inset) Comparison between the analytical result [solid line, Eq. (2)] and numerical simulation (squares) for Δ_{ST-} around $\theta = 0$. Here, the analytical expression fails due to the small in-plane Zeeman energies. (d) Comparison between the two contributions to Δ_{ST_-}.

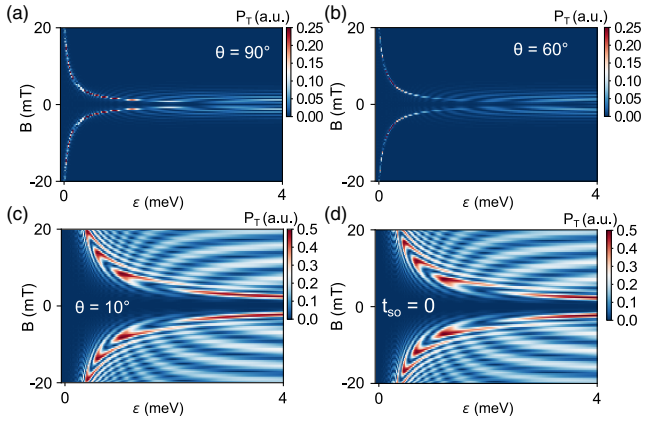

FIG. 4. Simulations of the funnel plots with the master equation approach using qutip. (a)–(c) Funnel for $\theta = 90°$, 60°, and 10°, respectively, showing the $S - T_-$ avoided crossing as an increased triplet return probability. The simulations take the model Hamiltonian with the experimentally extracted parameters as input and perform the time-evolution calculation returning the combined triplet return probability $(P_{T_+} + P_{T_-} + P_{T_0})$. The simulations reproduce the experimental data observed in Fig. 1. (d) A simulation with $t_{SO} = 0$ but with all the other values of the model as in (c) again reveals the butterfly shape of the $S - T_-$ avoided crossing.

$$\Delta_{ST_-} = \left|\Delta_{SO} \sin\left(\frac{\Omega}{2}\right) + \Delta E_Z \cos\left(\frac{\Omega}{2}\right)\right|, \tag{2}$$

where the spin-orbit splitting Δ_{SO} and the Zeeman splitting ΔE_Z due to anisotropic site-dependent g tensors read

$$\Delta_{SO} = t_y + i t_x \frac{g_\perp^+ \sin\theta}{\sqrt{(g_\parallel^+ \cos\theta)^2 + (g_\perp^+ \sin\theta)^2}}, \tag{3}$$

$$\Delta E_Z = \frac{\mu_B B}{4\sqrt{2}} \frac{(g_\parallel^- g_\perp^+ - g_\parallel^+ g_\perp^-)\sin(2\theta)}{\sqrt{(g_\parallel^+ \cos\theta)^2 + (g_\perp^+ \sin\theta)^2}}, \tag{4}$$

and $\Omega = \arctan(2\sqrt{2} t_C/\epsilon^*)$ is the mixing angle at the anticrossing. The analytical result (2) agrees well with the numerical results obtained by exact diagonalization of the system Hamiltonian for all θ except in a narrow region around $\theta = 0$ [$|\theta| \lesssim 2°$, inset of Fig. 3(c)]. We attribute these deviations to the small in-plane Zeeman energies which violate the assumption of an isolated two-level system made when deriving (2) (see Supplemental Material [17] Sec. VI). Because of the opposite sign g-factor corrections in the dots the Zeeman splitting ΔE_Z can be the dominant contribution to Δ_{ST_-}, exceeding the spin-orbit splitting by one order of magnitude at small angles. Even when the magnetic field has a large out-of-plane component, the effect of different g factors can contribute crucially to Δ_{ST_-} [Fig. 3(d)].

The extracted Δ_{ST_-} in Fig. 3(c) can be fit by the model with t_x and t_y as free parameters and t_C, $g_\perp^+$, $g_\perp^-$, $g_\parallel^+$, $g_\parallel^-$ extracted from previous measurements. Between −25° and 25° the splitting seems to drop to zero as the Landau-Zener assumptions of diabatic return sweeps are not met and an extraction of Δ_{ST_-} is not accurate. The black dashed line corresponds to the maximum Δ_{ST_-} that allows a diabatic passage with a rise time of 2 ns of our pulses $(P_{LZ,max} = 0.99 = \exp[-(2\pi\Delta_{ST,max}^2/\hbar v)])$. The model fits the dark blue data points with $t_x = 129.0 \pm 18.0$ and $t_y = -369.8 \pm 13.8$ neV, yielding the total spin-flip tunneling element $t_{SO} = \sqrt{t_x^2 + t_y^2} = 392.0$ neV.

Having characterized all the elements in the Hamiltonian from independent measurements we can now reproduce the funnel measurements in Fig. 1 (Fig. 4). In particular the sharper line at $\theta = 60°$ [Fig. 4(b)] as well as the $S - T_-$ oscillations for $\theta = 10°$ [Fig. 4(c)] reflect what we observe in the data. Even with $t_{SO} = 0$ the in-plane g-factor difference induces $S - T_-$ oscillations [Fig. 4(d)] further confirming its dominant role in determining the size of Δ_{ST_-}.

In conclusion, we have demonstrated that the g-tensor anisotropy and, in particular, the in-plane g-factor

difference can lead to a considerable contribution to $\Delta_{ST\_}$ in the in-plane direction. However, Landau-Zener sweeps and singlet-triplet oscillations measured in different magnetic field directions allowed us to distinguish the Zeeman induced coupling from the spin-orbit induced coupling and, thereby, infer the magnitude and orientation of t_{SO}. We reconstructed the experimental data in our simulations confirming the validity of our theoretical model. This understanding of the interplay between t_{SO} and the in plane g-factor difference opens the possibility to operate hole singlet-triplet qubits at sweet spots, for example with orthogonal axis [34]. Our work, therefore, provides important insight into the spin-orbit interaction of hole spin double quantum dot devices and lays the foundation for the design of future hole spin qubit experiments.

This research was supported by the Scientific Service Units of ISTA through resources provided by the MIBA Machine Shop and the nanofabrication facility. This project has received funding from the European Union's Horizon 2020 research and innovation program under the Marie Skłodowska-Curie Grant Agreement No. 844511, No. 75441, and by the FWF-P 30207, I05060, and M 3032-N projects. A. B. acknowledges support from the EU Horizon-2020 FET project microSPIRE, ID: 766955. P. M. M. and G. B. acknowledge funding by the Deutsche Forschungsgemeinschaft (DFG—German Research Foundation) under Project No. 450396347. This work was supported by the Royal Society (URF\R1\191150) and the European Research Council (Grant Agreement No. 948932), N. A. acknowledges the use of the University of Oxford Advanced Research Computing (ARC) facility.

*daniel.jirovec@ista.ac.at
†philipp.mutter@uni-konstanz.de

[1] V. N. Golovach, M. Borhani, and D. Loss, Electric-dipole-induced spin resonance in quantum dots, Phys. Rev. B **74**, 165319 (2006).
[2] D. V. Bulaev and D. Loss, Electric Dipole Spin Resonance for Heavy Holes in Quantum Dots, Phys. Rev. Lett. **98**, 097202 (2007).
[3] X. Wu *et al.*, Two-axis control of a singlet-triplet qubit with an integrated micromagnet, Proc. Natl. Acad. Sci. U.S.A. **111**, 11938 (2014).
[4] J. Yoneda *et al.*, A quantum-dot spin qubit with coherence limited by charge noise and fidelity higher than 99.9%, Nat. Nanotechnol. **13**, 102 (2018).
[5] R. Maurand *et al.*, A CMOS silicon spin qubit, Nat. Commun. **7**, 13575 (2016).
[6] A. Crippa *et al.*, Electrical Spin Driving by g -Matrix Modulation in Spin-Orbit Qubits, Phys. Rev. Lett. **120**, 137702 (2018).
[7] H. Watzinger, J. Kukučka, L. Vukušić, F. Gao, T. Wang, F. Schäffler, J.-J. Zhang, and G. Katsaros, A germanium hole spin qubit, Nat. Commun. **9**, 3902 (2018).
[8] N. W. Hendrickx, W. I. L. Lawrie, L. Petit, A. Sammak, G. Scappucci, and M. Veldhorst, A single-hole spin qubit, Nat. Commun. **11**, 3478 (2020).
[9] N. W. Hendrickx, D. P. Franke, A. Sammak, G. Scappucci, and M. Veldhorst, Fast two-qubit logic with holes in germanium, Nature (London) **577**, 487 (2020).
[10] F. N. M. Froning, L. C. Camenzind, O. A. H. van der Molen, A. Li, E. P. A. M. Bakkers, D. M. Zumbühl, and F. R. Braakman, Ultrafast hole spin qubit with gate-tunable spin–orbit switch functionality, Nat. Nanotechnol. **16**, 308 (2021).
[11] K. Wang *et al.*, Ultrafast operations of a hole spin qubit in ge quantum dot, Nat. Commun. **13**, 206 (2022).
[12] R. Moriya *et al.*, Cubic Rashba Spin-Orbit Interaction of a Two-Dimensional Hole Gas in a Strained-ge/SiGeQuantum Well, Phys. Rev. Lett. **113**, 086601 (2014).
[13] S. Bosco, M. Benito, C. Adelsberger, and D. Loss, Squeezed hole spin qubits in ge quantum dots with ultrafast gates at low power, Phys. Rev. B **104**, 115425 (2021).
[14] Z. Wang, E. Marcellina, A. R. Hamilton, J. H. Cullen, S. Rogge, J. Salfi, and D. Culcer, Optimal operation points for ultrafast, highly coherent ge hole spin-orbit qubits, npj Quantum Inf. **7**, 54 (2021).
[15] D. Jirovec *et al.*, A singlet-triplet hole spin qubit in planar Ge, Nat. Mater. **20**, 1106 (2021).
[16] R. J. Schoelkopf, P. Wahlgren, A. A. Kozhevnikov, P. Delsing, and D. E. Prober, The radio-frequency single-electron transistor (RF-SET): A fast and ultrasensitive electrometer, Science **280**, 1238 (1998).
[17] See Supplemental Material at http://link.aps.org/supplemental/10.1103/PhysRevLett.128.126803 for pulse calibrations, additional data and details of the theoretical model derivation, which includes Ref. [18–23].
[18] X. Marie, T. Amand, P. Le Jeune, M. Paillard, P. Renucci, L. E. Golub, V. D. Dymnikov, and E. L. Ivchenko, Hole spin quantum beats in quantum-well structures, Phys. Rev. B **60**, 5811 (1999).
[19] A. V. Trifonov *et al.*, Strong enhancement of heavy-hole landé factor q in ingaas symmetric quantum dots revealed by coherent optical spectroscopy, arXiv:2103.13653.
[20] G. Granger, G. C. Aers, S. A. Studenikin, A. Kam, P. Zawadzki, Z. R. Wasilewski, and A. S. Sachrajda, Visibility study of $S - T_+$ landau-zener-stückelberg oscillations without applied initialization, Phys. Rev. B **91**, 115309 (2015).
[21] L. A. Orona, J. M. Nichol, S. P. Harvey, C. G. L. Bøttcher, S. Fallahi, G. C. Gardner, M. J. Manfra, and A. Yacoby, Readout of singlet-triplet qubits at large magnetic field gradients, Phys. Rev. B **98**, 125404 (2018).
[22] J. Danon and Y. V. Nazarov, Pauli spin blockade in the presence of strong spin-orbit coupling, Phys. Rev. B **80**, 041301(R) (2009).
[23] V. N. Golovach, A. Khaetskii, and D. Loss, Phonon-Induced Decay of the Electron Spin in Quantum Dots, Phys. Rev. Lett. **93**, 016601 (2004).
[24] J. R. Petta, Coherent manipulation of coupled electron spins in semiconductor quantum dots, Science **309**, 2180 (2005).
[25] L. D. Landau, Zur theorie der energieübertragung. II., Phys. Sov. Union **2**, 46 (1932).
[26] C. Zener, Non-adiabatic crossing of energy levels, Proc. R. Soc. A **137**, 696 (1932).

[27] S. Shevchenko, S. Ashhab, and F. Nori, Landau–zener–stückelberg interferometry, Phys. Rep. **492**, 1 (2010).
[28] J. R. Petta, H. Lu, and A. C. Gossard, A coherent beam splitter for electronic spin states, Science **327**, 669 (2010).
[29] D. L. Craig *et al.*, Bridging the reality gap in quantum devices with physics-aware machine learning, arXiv:2111.11285.
[30] R. Winkler, *Spin—Orbit Coupling Effects in Two-Dimensional Electron and Hole Systems* (Springer, Berlin, Heidelberg, 2003).
[31] D. Stepanenko, M. Rudner, B. I. Halperin, and D. Loss, Singlet-triplet splitting in double quantum dots due to spin-orbit and hyperfine interactions, Phys. Rev. B **85**, 075416 (2012).
[32] J. Fischer, W. A. Coish, D. V. Bulaev, and D. Loss, Spin decoherence of a heavy hole coupled to nuclear spins in a quantum dot, Phys. Rev. B **78**, 155329 (2008).
[33] P. M. Mutter and G. Burkard, Natural heavy-hole flopping mode qubit in germanium, Phys. Rev. Research **3**, 013194 (2021).
[34] P. M. Mutter and G. Burkard, All-electrical control of hole singlet-triplet spin qubits at low-leakage points, Phys. Rev. B **104**, 195421 (2021).

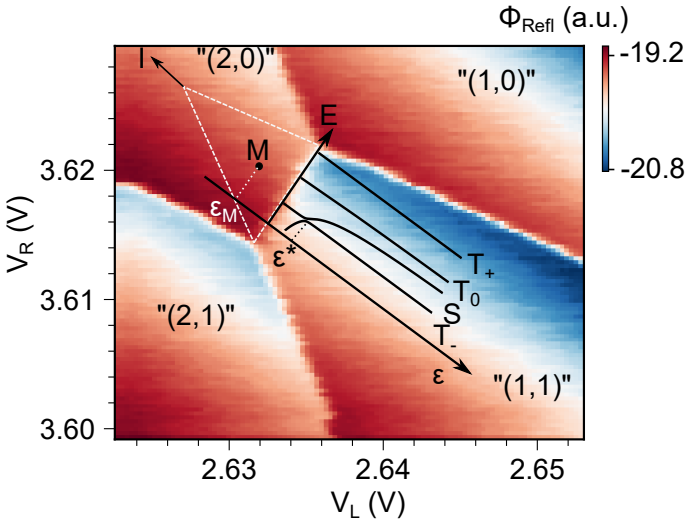

FIG. S1. The effective hole numbers are labelled "(n_L, n_R)". The real hole number is $(n_L+2, 2n+n_R)$ since we do not know the exact number of holes in the right dot. The dashed triangle marks the region in which Pauli spin blockade occurs and the measurement point (M) is located at the center of it at $\epsilon = \epsilon_M$. "I" marks the initialization point. The dispersion relation is overlaid on top of the "(1,1)" region. The avoided $S - T_-$ crossing occurs at $\epsilon = \epsilon^*$

Supplementary: Dynamics of Hole Singlet-Triplet Qubits with Large g-Factor Differences

I. STABILITY DIAGRAM, PULSING, TUNNEL COUPLING

The stability diagram around the transition of interest is reported in Fig. S1. The effective hole numbers are labelled "(n_L, n_R)" while the real hole number is (n_L+2, n_R+2n). The dispersion relation is overlaid and highlights the 4 states involved in the dynamics of the system. When pulsing we initialize (I) deep in "(2,0)" with a short pulse knowing that the short relaxation time T_1 ensures decay to a singlet. Only for the in-plane field direction this is not true as is further discussed below.

We extract the tunnel coupling from exchange oscillations. A typical pulse sequence to probe the exchange interaction J is depicted in the inset of Fig. S2a. After initialization in $S(2,0)$ the system is pulsed rapidly to large ϵ and left to evolve for a time corresponding to a $\pi/2$ rotation around the x-axis of the Bloch-sphere. A subsequent pulse at lower ϵ for a time τ_S increases the exchange interaction $J(\epsilon) = \sqrt{\frac{\epsilon^2}{4} + 2t_C^2} - \frac{\epsilon}{2}$. Therefore, the oscillation frequency $f = \sqrt{J(\epsilon)^2 + (g_\perp^- \mu_B B)^2}$ will reflect the change in J and increase for lower ϵ. The fit in Fig. S2, therefore, allows to extract the tunnel coupling. As the coherence time for very low ϵ tends to 0, all the points at $\epsilon < \epsilon^*$ are not considered in the fit. ϵ^* is highlighted by the black arrow where the $S - T_-$ mixing is prominently visible.

II. SINGLET-TRIPLET DYNAMICS FOR SMALL ANGLES

We probe singlet-triplet oscillations at small angles by rapidly pulsing to large ϵ and observing the signal of the returned state. In Fig. S3a the resulting oscillation pattern is displayed for $\theta = 0°$. The FFT in S3b reveals several frequency components. The dotted lines are extracted from our model and the corresponding dispersion relation is depicted in S3c. The colored arrows mark the transitions we actually observe in the FFT plot. The singlet-triplet oscillation and FFT plots for $\theta = 5, 10, 20$ and $30°$ are further depicted in Fig. S4. We generally find a good agreement with our theoretical model.

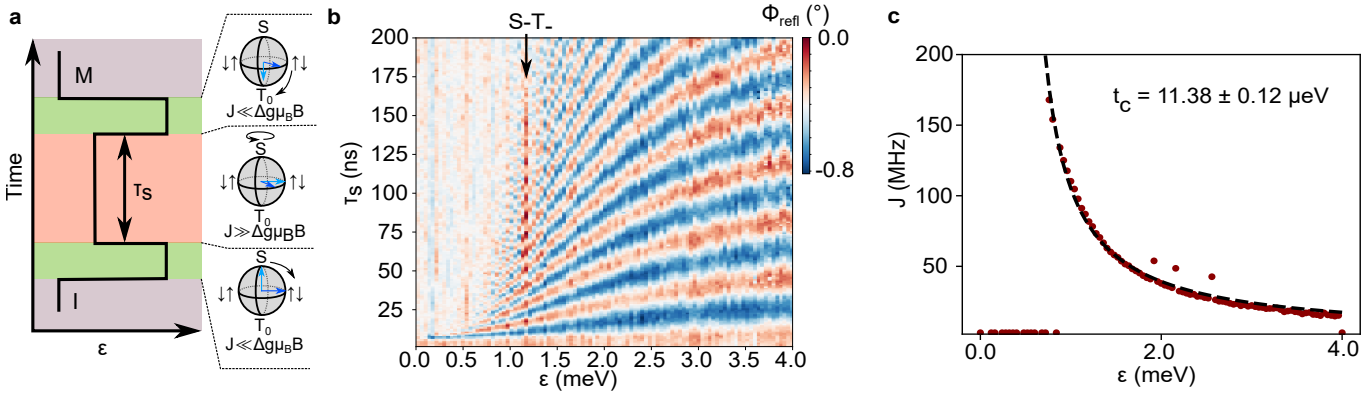

FIG. S2. a) The pulse sequence to obtain exchange oscillations features two short pulses at high ϵ (green) where the exchange interaction $J \ll \Delta g \mu_B B$. Here, the system rotates around the x-axis of the Bloch sphere. The exchange interaction can be turned on by pulsing to lower ϵ (orange). Here $J \gg g_{\perp}^{-} \mu_B B$ and the system evolves around the z-axis of the Bloch sphere. b) The exchange oscillations as a function of ϵ and separation time τ_S at $B_{\perp} = 1\,\mathrm{mT}$ display the expected frequency increase for lower detuning as the exchange interaction becomes dominant. Around 1.2 meV the $S - T_{-}$ avoided-crossing is visible as an increase in triplet return signal (red). c) The magnitude of J in MHz can be fit by $J(\epsilon, t_C) = \sqrt{\frac{\epsilon^2}{4} + 2t_C^2} - \frac{\epsilon}{2}$ (black dashed line) and we extract $t_C = 11.38\,\mu\mathrm{eV}$.

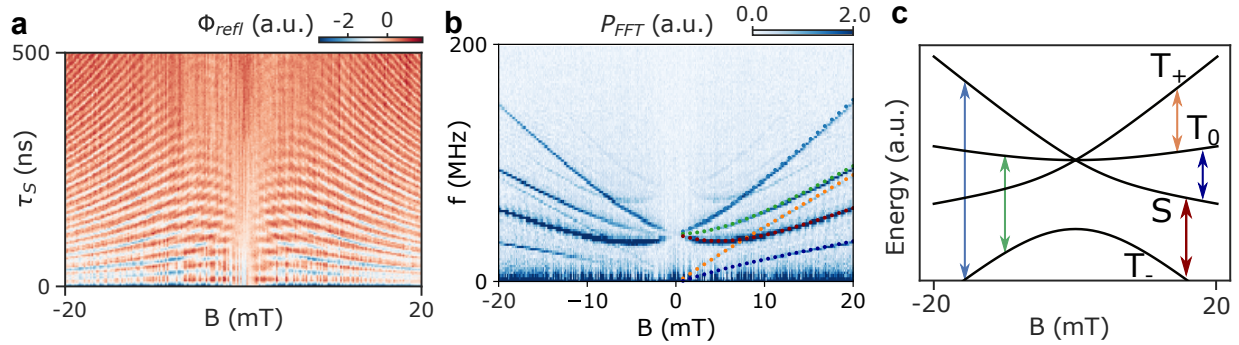

FIG. S3. a) Singlet oscillations as a function of in-plane magnetic field and free evolution time under fast pulsing revealing a complicated oscillation pattern. b) A FFT of a) unveils many frequency components. The dotted lines are fits to the transition frequencies highlighted in c). We find good agreement between the data and the model. An additional set of lines appears at slightly higher frequencies which we attribute to spectral leakage due to the imperfect initialization [S1]. c) The arrows point out the transition frequencies between the eigenstates for the in-plane dispersion relation.

III. $S - T_{-}$ AVOIDED-CROSSING AS A FUNCTION OF MAGNETIC FIELD DIRECTION

We report the $S - T_{-}$ avoided-crossing for different magnetic field directions in Fig. S5. For the out-of-plane direction the typical funnel shape can clearly be observed. Towards the in-plane direction the $S - T_{-}$ avoided-crossing evolves into an oscillation pattern suggesting a large coupling term between S and T_{-}. This anisotropy, which follows the g-factor anisotropy of confined HH states, indicates a dependence related to the Zeeman terms in H_{tot}. Indeed, our model can reproduce the plots assuming $g_{\parallel}^{-} > g_{\parallel}^{+}$.

We furthermore report the effective level velocity $v = |\frac{dJ(\epsilon)}{d\epsilon}|_{\epsilon=\epsilon^*} \frac{\Delta\epsilon}{\tau_R}$ with $\Delta\epsilon = 4\,\mathrm{meV}$, $\tau_R = 2\,\mathrm{ns}$ as a function of the magnetic field angle θ for a magnetic field strength of 20 mT (Fig. S6). Towards the in-plane direction the velocity is reduced as the Zeeman splitting is lowered due to the g-factor anisotropy. As a result, for small angles, the shortest possible ramp time does not allow a diabatic passage over the avoided crossing as pointed out in Fig. **??**b. Incidentally, this is a favorable property for single spin qubits where fast initialization in the $|\downarrow\downarrow\rangle$ state is required. Indeed, for $\theta = 0$ the ground state in (1,1) can be initialized with fidelity $F = 1 - P_{LZ} \approx 1$ at a ramp time of 20 ns (Fig. S6).

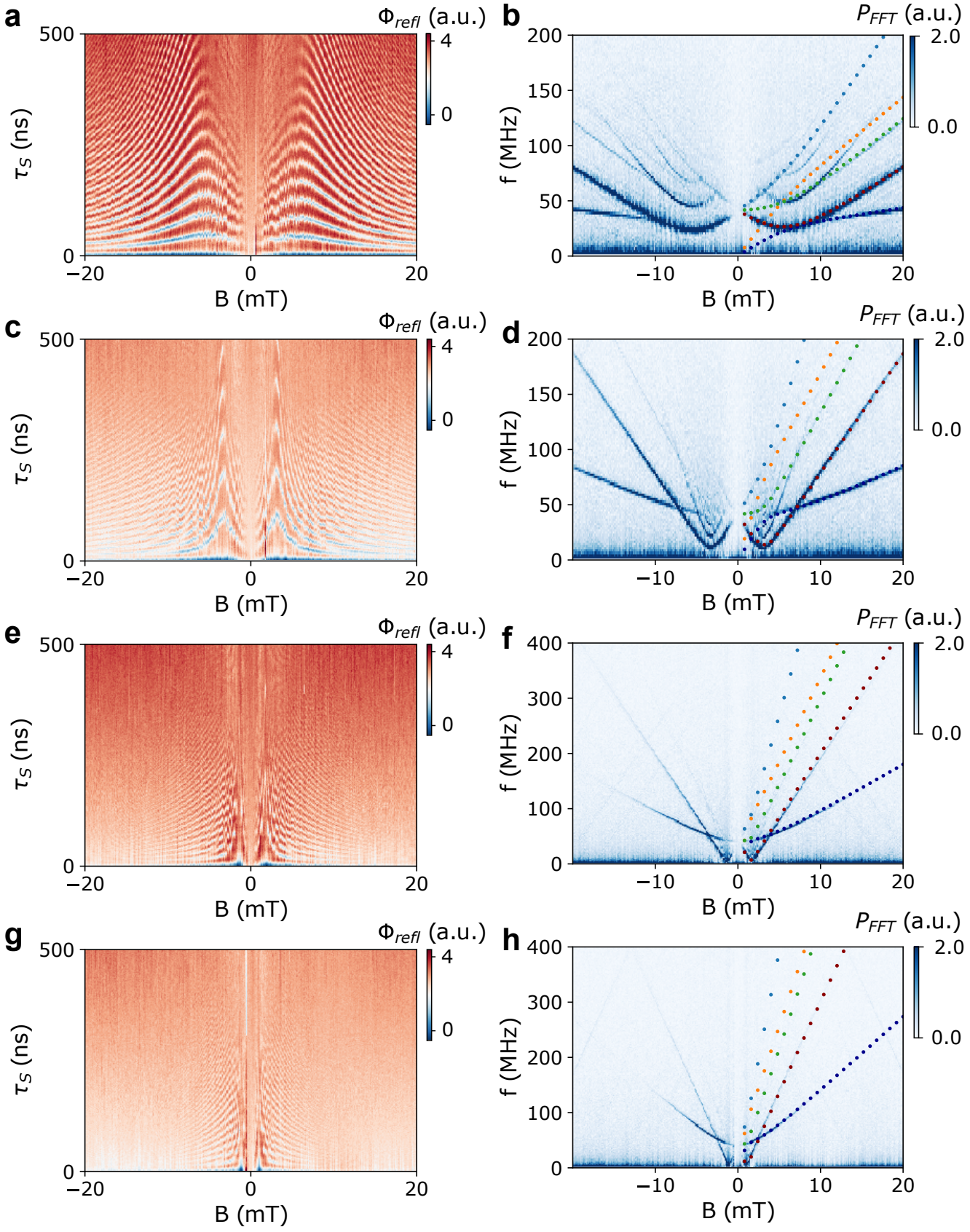

FIG. S4. Singlet-triplet oscillations as a function of B at different θ. a) Oscillations at $\theta = 5°$. b) FFT of a) with overlaid frequency lines for positive fields as extracted from the model. c) Oscillations at $\theta = 10°$. d) FFT of c) with overlaid frequency lines as extracted from the model. e) Oscillations at $\theta = 20°$. f) FFT of e) with overlaid frequency lines as extracted from the model. g) Oscillations at $\theta = 30°$. h) FFT of g) with overlaid frequency lines as extracted from the model.

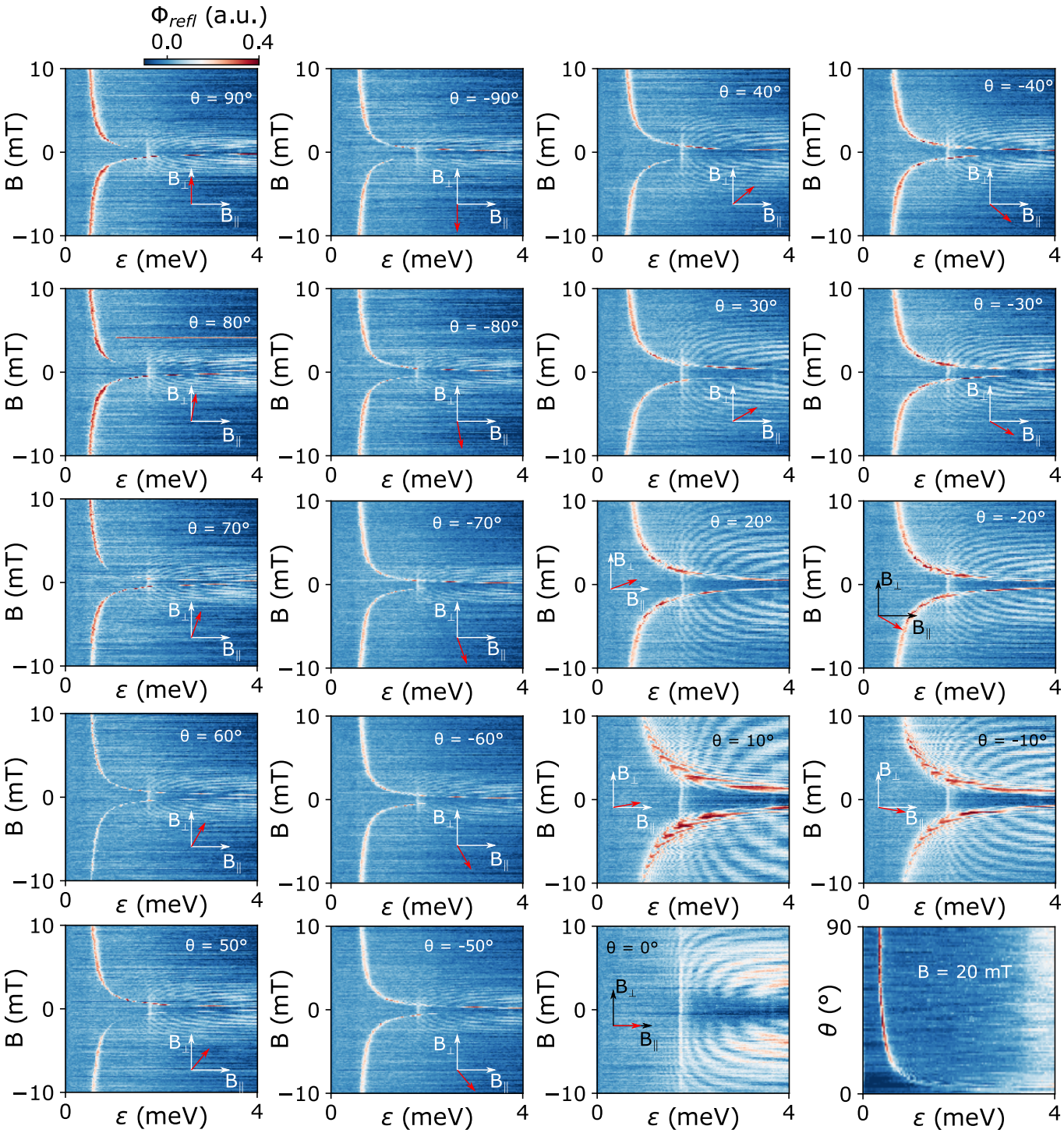

FIG. S5. $S - T_-$ avoided-crossing funnel for different angles for $\tau_S = 250\,\mathrm{ns}$. Clearly the funnel is well defined for out-of-plane fields and evolves into an oscillation pattern for in-plane fields. This suggests a dependence stemming from the g-factor anisotropy of HH states. In fact, our model fits the experimentally observed funnel shapes with $g_\perp^+ = 12$, $g_\perp^- = 2.05$, $g_\parallel^+ = 0.1$, $g_\parallel^- = 0.43$. Moreover, the spin-orbit vector pointing along $\theta = 60°$ gives rise to an asymmetry between the sharpness of the funnel at $+60°$ and $-60°$, also confirmed by single Landau-Zener sweeps. The bottom right plot shows the $S - T_-$ avoided-crossing at 20 mT for positive angles. This is used to calibrate the pulse amplitude necessary to overcome the $S - T_-$ avoided-crossing ($\epsilon > \epsilon^*$) in the single Landau-Zener sweeps (see Fig. 3b of the main text).

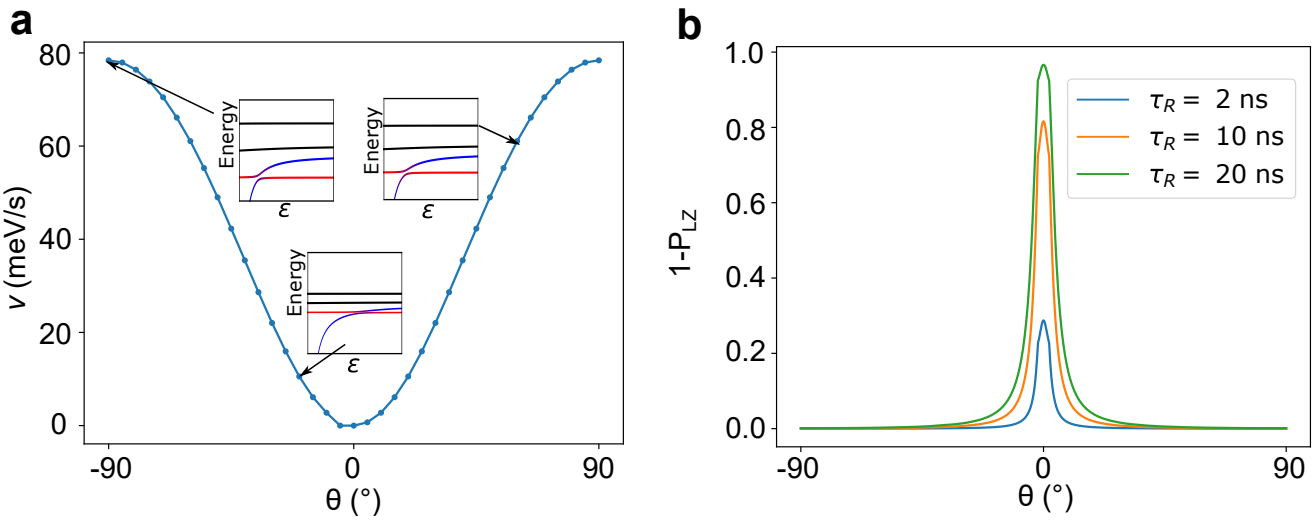

FIG. S6. a) Velocity v as a function of θ for a magnetic field strength of 20 mT. Because of the g-factor anisotropy the Zeeman energy in the in-plane direction is lower. Consequently the velocity is reduced as $|dJ/d\epsilon|_{\epsilon=\epsilon^*}$ becomes smaller. The inset shows the simulated energy dispersion for the angles highlighted by the black arrows. For in-plane fields the avoided crossing clearly shifts to larger ϵ thereby reducing the effective level velocity. b) $1 - P_{LZ}$ as a function of θ for different ramp times. Hence, the g-factor difference in the in-plane direction allows fast and high fidelity initialization for single spin qubits.

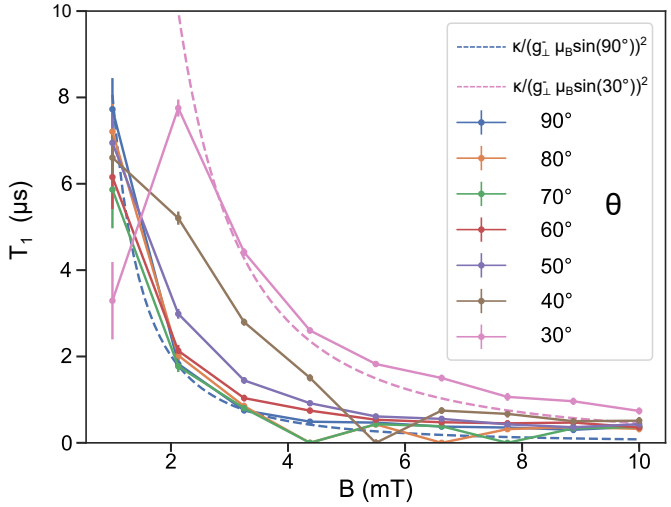

FIG. S7. Relaxation time of the $|T_0\rangle$ state as a function of magnetic field strength and angle. In contrast to the decay of the T_- state the relaxation of the T_0 state is proportional to $\kappa/\Delta E_Z^2$ (dashed lines) wiht κ a proportionality constant. T_1 generally decreases for larger magnetic fields. Only for $\theta = 30°$ the relaxation time maximizes at 2 mT. This occurs because for lower magnetic fields the presence of the $S - T_-$ avoided crossing lowers the T_0 return probability as a diabatic passage can not be achieved with the finite rise time of our AWG. For angles $\theta < 30°$ no diabatic passage can be achieved. Therefore we cannot extract T_1 of the T_0 state.

IV. DECAY OF T_0 STATE

The relaxation time of the T_0 state does not depend on the SOI (Eq. S15)and, therefore, displays a different anisotropy than the relaxation for the T_- state. To probe this, we perform diabatic pulses and fit the decay of the return signal to $\Phi_{refl}(\tau_M = 0)\exp\left(-\frac{\tau_M}{T_1}\right)$. As shown in Fig. S7 the relaxation time follows $\approx \frac{1}{g_\perp^- \mu_B B \sin\theta}^2$ and is generally $< 10\,\mu$s making read-out at large fields challenging. Therefore, shelved read-out [S2] could be harvested where the read-out distinguishes between S and T_-. At $\theta = 60°$ the relaxation of the T_- state is maximised offering a sweet spot for shelved read-out.

V. INITIALIZATION AND SPECTRAL LEAKAGE

The fast Fourier transform plots in Fig. S3 and Fig. S4 display additional frequency components not predicted by our model which are especially evident at $\theta = 5°$ and $10°$ and can be attributed to improper initialization of the singlet state prior to a pulse. In [S1] a similar system is analyzed and a general formula for the singlet return probability P_S of non-properly initialized state (a superposition of S and T_-) is extracted as

$$P_S = P'_S P + [1 - P'_S](1 - P), \tag{S1}$$

where P is the return probability with correct singlet initialization and

$$P'_S = \frac{P \exp\left(-\frac{\tau_M}{T_1}\right) - 1}{(2P - 1)\exp\left(-\frac{\tau_M}{T_1}\right) - 1}. \tag{S2}$$

Here, τ_M is the measurement time and T_1 is the relaxation time of the T_- state in the read-out point. It is clear that for $\tau_M \gg T_1$ we find $P_S = P$. However, when $\tau_M \approx T_1$ the singlet return probability deviates significantly from P. In Fig. S8a we show a line trace of Fig. S4 at $\theta = 5°$ and $B = 8.5\,\mathrm{mT}$. We clearly see that the oscillations are not sinusoidal. Fig. S8b displays the FFT of the line trace and 3 distinct peaks can be observed. However, more peaks are present but buried in the background. Fig. S8c shows a simulation of the time evolution of the state. The red trace assumes perfect initialization whereas the blue trace depicts the corrected singlet return probability according to Eq. S1 and S2 with $\tau_M \approx T_1$. The blue trace indeed resembles what we measure. Furthermore, we inspect the FFT of the simulated data and find that indeed for the improperly initialized curve we observe additional frequency components. In the red trace we find only the frequency components corresponding to the transitions highlighted in Fig. S3 of the main text. The FFT plot extracted from the simulation of the properly initialized state is depicted as a function of magnetic field in Fig. S8e. On the other hand, the improperly initialized simulated FFT is plotted in Fig. S8f. Here, several additional lines are clearly visible and follow what we measure in Fig. S4b albeit with altered Fourier amplitudes.

VI. THE MODEL

We consider a tunnel coupled double quantum dot in the presence of an external magnetic field and the spin-orbit interaction (SOI). For the small magnetic fields considered in this work, $B \lesssim 20$ mT, we may neglect orbital effects arising from the canonical momentum and model the system by the Hamiltonian

$$H_{tot} = H_{orb} + H_Z + H_{SO}, \tag{S3}$$

where H_Z is the Zeeman Hamiltonian and H_{SO} describes the SOI. The orbital part H_{orb} reads

$$H_{orb} = \epsilon|S_{20}\rangle\langle S_{20}| + \sqrt{2}t_C\left(|S_{11}\rangle\langle S_{20}| + |S_{20}\rangle\langle S_{11}|\right), \tag{S4}$$

where $|S_{20}\rangle$ is the singlet with double occupancy in the left dot which is detuned by an amount ϵ from the $(1,1)$ configuration, t_C is the tunnel element in the one-particle picture, and $|S_{11}\rangle$ is the singlet with one hole in each dot. Diagonalizing (S4) yields the hybridized singlet states

$$|S_E\rangle = \cos\left(\frac{\Omega}{2}\right)|S_{20}\rangle + \sin\left(\frac{\Omega}{2}\right)|S_{11}\rangle, \tag{S5a}$$

$$|S_G\rangle = \cos\left(\frac{\Omega}{2}\right)|S_{11}\rangle - \sin\left(\frac{\Omega}{2}\right)|S_{20}\rangle, \tag{S5b}$$

where $\Omega = \arctan\left(2\sqrt{2}t_C/\epsilon\right)$ is the orbital mixing angle and the corresponding energies are $E(S_{E/G}) = \epsilon/2 \pm \sqrt{\epsilon^2/4 + 2t_C^2}$. In the following we consider a regime where the excited singlet is far detuned and may be neglected. Defining $|S\rangle \equiv |S_G\rangle$, we may focus on the four dimensional space spanned by the states $|S\rangle$, $|T_+\rangle$, $|T_0\rangle$ and $|T_-\rangle$, where $|T_{0,\pm}\rangle$ denote the triplet states in the (1,1) configuration.

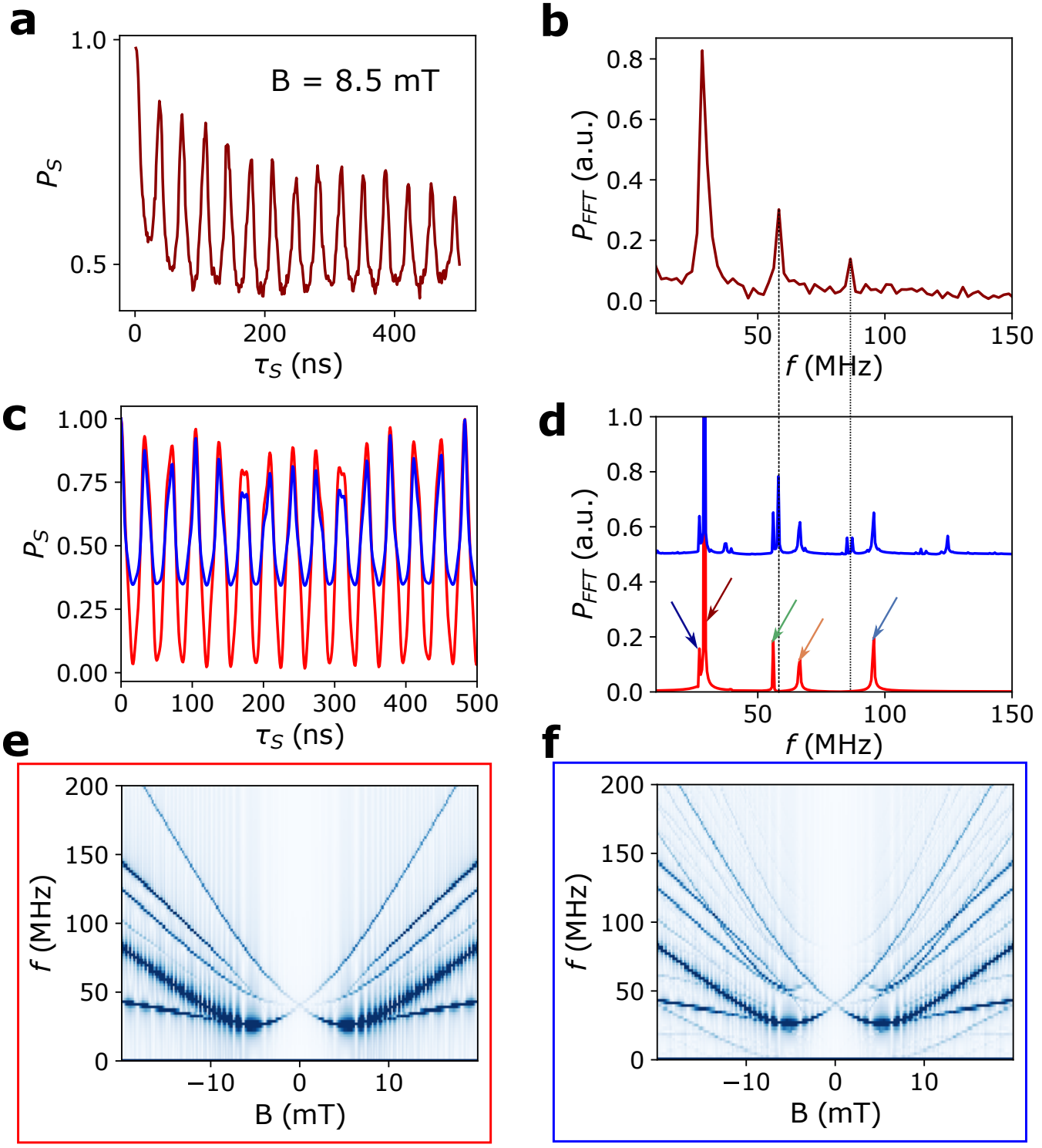

FIG. S8. a) Line trace at 8 mT from Fig. S4a featuring a non-sinusoidal oscillation pattern. b) FFT of a) highlighting its frequency components. c) Simulated time evolution for the conditions in a) with proper initialization in a singlet (red) and improper initialization (blue). d) FFT of c) highlighting the frequency components of the blue and red trace (blue is offset for clarity). Comparing the 2 curves we notice additional frequency components arising in the blue one which can be mapped to the observed spectral peaks of b). The red and blue trace, however, both display peaks at the transition frequencies expected from our model. e) FFT of the simulated time evolution with proper initialization. All the transitions highlighted in Fig. S3c are visible. f) FFT of the simulated time evolution under improper initialization. The additional frequency lines resemble what we measure in Fig. S4b.

For a magnetic field of magnitude B and angle θ as measured from the plane defined by the heterostructure, the Zeeman Hamiltonian H_Z reads,

$$\begin{aligned} H_Z = \frac{\mu_B B}{2}\Bigg\{ &\sin\theta\left[\sum_{\pm} \pm g_\perp^+ |T_\pm\rangle\langle T_\pm| + g_\perp^- \left(|S\rangle\langle T_0| + |T_0\rangle\langle S|\right)\cos\left(\frac{\Omega}{2}\right)\right] \\ &+\frac{\cos\theta}{\sqrt{2}}\left[\sum_{\pm}\left(g_\parallel^+ |T_0\rangle\langle T_\pm| \mp g_\parallel^- |S\rangle\langle T_\pm|\cos\left(\frac{\Omega}{2}\right) + \text{H.c.}\right)\right]\Bigg\}, \end{aligned} \tag{S6}$$

where $g_j^\pm = g_j^L \pm g_j^R$. Note that the axes are labelled such that y is the double quantum dot axis, and the magnetic field is applied in the x-z-plane.

Finally, we consider a SOI parametrized by an in-plane spin-orbit vector, $\mathbf{t}_{SO} = (t_x, t_y, 0)$, where all entries are real. Such in-plane spin-flip tunneling terms stem from the cubic Rashba SOI [S3], while this type of SOI does not induce out-of-plane terms t_z. Consequently, the spin-orbit Hamiltonian H_{SO} reads,

$$H_{SO} = \sin\left(\frac{\Omega}{2}\right)\sum_{\pm}(t_x \pm i t_y)|T_\pm\rangle\langle S| + \text{H.c.}, \tag{S7}$$

An appropriate basis for studying the singlet-triplet anticrossing is given by the eigenstates of the total Hamiltonian (S3) for equal g-factors and in the absence of the SOI. Transforming the total Hamiltonian in the presence of the SOI and g-factor differences into this basis, we find for the singlet-triplet splitting,

$$\Delta_{ST_-} = \left|\Delta_{SO}\sin\left(\frac{\Omega}{2}\right) + \Delta E_Z\cos\left(\frac{\Omega}{2}\right)\right|, \tag{S8}$$

where the spin-orbit splitting Δ_{SO} and the Zeeman splitting ΔE_Z are given by

$$\Delta_{SO} = t_y - i t_x \frac{g_\perp^+ \sin\theta}{\sqrt{(g_\parallel^+\cos\theta)^2 + (g_\perp^+\sin\theta)^2}}, \tag{S9a}$$

$$\Delta E_Z = \frac{\mu_B B}{4\sqrt{2}}\frac{\left(g_\parallel^- g_\perp^+ - g_\parallel^+ g_\perp^-\right)\sin(2\theta)}{\sqrt{(g_\parallel^+\cos\theta)^2 + (g_\perp^+\sin\theta)^2}}. \tag{S9b}$$

In Landau-Zener measurements the mixing angle Ω is a function of the detuning at the anticrossing between the singlet and the low-energy polarized triplet, which is described by the equation

$$\frac{\epsilon}{2} - \sqrt{\frac{\epsilon^2}{4} + 2t_C^2} = -\frac{\mu_B B}{2}G(\theta), \tag{S10}$$

where $G(\theta) = \sqrt{(g_\parallel^+\cos\theta)^2 + (g_\perp^+\sin\theta)^2}$. Rearranging gives the detuning at which the anticrossing is located,

$$\epsilon_* = \frac{8t_C^2 - \left(\mu_B B G(\theta)\right)^2}{2\mu_B B G(\theta)}, \tag{S11}$$

and consequently the mixing angle at the anticrossing reads

$$\Omega_* = \Omega(\epsilon_*) = \arctan\left(\frac{4\sqrt{2}t_C\mu_B B G(\theta)}{8t_c^2 - (\mu_B B G(\theta))^2}\right). \tag{S12}$$

In Fig. **??**d we show a comparison between the analytical result for Δ_{ST_-} evaluated at the detuning at the anticrossing and simulated results obtained by exact numerical diagonalization of the total system Hamiltonian (S3). For the latter, we obtain the splitting as the minimum difference between the two lowest eigenenergies. We find excellent agreement for all angles except in a narrow region around $\theta = 0$. The dip predicted by the analytical formula is not present in the simulations. We attribute this deviation to the small in-plane Zeeman energies $\sim g_\parallel^+$ which violate the assumption of a well separated two-level system. In this case the splitting is not given by the simple expression (S8) which describes the coupling between the ground state singlet and the low-energy polarized triplet. Instead, the contributions of the remaining two triplet states must be taken into account near $\theta = 0$, and the coupling is altered.

VII. SPIN-ORBIT VECTOR, FIELD AND LENGTH

In Eq. (S7) we model the SOI using the spin-orbit vector $\mathbf{t}_{\rm SO} = (t_x, t_y, t_z)$ [S4] which contains genuine spin-flip tunneling terms. In our structure we consider an in-plane spin-orbit vector, but different forms with $t_z \neq 0$ are possible in other systems. The most general effective form in the basis $\mathcal{B}$ defined in Sec. VI is

$$H_{SO} = \sin\left(\frac{\Omega}{2}\right)\left(i\sqrt{2}t_z|T_0\rangle\langle S| + \sum_{\pm}(t_x \pm it_y)|T_\pm\rangle\langle S| + \text{H.c.}\right). \tag{S13}$$

Often, however, the SOI is parametrized by a spin-orbit field $\mathbf{M}_{SO}^d$ in dot $d \in \{L, R\}$,

$$H_{SO} = \frac{\mu_B}{2}\sum_d \mathbf{M}_{SO}^d \cdot \boldsymbol{\sigma}^d, \tag{S14}$$

where $\boldsymbol{\sigma}^d$ is a vector containing the Pauli matrices in dot d. A general argument shows that the spin-orbit vector $\mathbf{t}_{SO}$ cannot be mapped to the spin-orbit field $\mathbf{M}_{SO}$. On the one hand, the Hamiltonian in Eq. (S7) is time reversal invariant while the Zeeman type Hamiltonian (S14) with a real spin-orbit field is not. On the other hand, a complex spin-orbit field would make (S14) non Hermitian, and hence the two quantities $\mathbf{t}_{SO}$ and $\mathbf{M}_{SO}$ cannot be related. Taking the spin-orbit field to be a function of the crystal momenta, $\mathbf{M}_{SO}^d(\mathbf{k})$, can restore time reversal symmetry but is not an appropriate description for the confined hole spin states considered here. Another quantity is based on an effective approach to first order in the SOI, explicitly taking into account phonons [S5],

$$\mathbf{M}_{SO}^d = 2\mathbf{B} \times \boldsymbol{\Omega}_{SO}^d, \tag{S15}$$

where $\mathbf{B}$ is the applied magnetic field, and $\boldsymbol{\Omega}_{SO}$ contains the effect of the SOI in dot d. However, with this definition one has $\mathbf{M}_{SO} = 0$ at zero magnetic field, in contrast to Eq. (S7) which is independent of the magnetic field. Rather, a Zeeman term (S14) with a spin-orbit field of the form (S15) complements the spin-flip tunneling terms appearing in the spin-orbit vector with additional intra-dot processes stemming from higher orbital contributions. These are expected to be negligible when the orbital energies $\hbar\omega_{x,y}$ are large compared to the spin-orbit parameters (in the present system we find $|\mathbf{t}_{SO}| \lesssim 500$ neV, $\hbar\omega_{x,y} \sim 1$ meV).

Yet another quantity commonly used in the literature is the spin-orbit length l_{SO}. It is shown in Ref. [S6] that the spin-conserving and spin-flip tunneling terms in a Ge double quantum dot with cubic Rashba SOI and a locally harmonic double quantum well potential are given by

$$\begin{aligned} t_C &= \frac{3N\gamma}{4}\left(\hbar\omega_0 + \frac{d^2 m\omega_0^2}{4}\right), \\ t_{SO} &= \lambda_R N(S-\gamma)\frac{d^3 m^3 \omega_0^3}{4}, \end{aligned} \tag{S16}$$

where $\hbar\omega_0$ is the in-plane confinement energy, m is the in-plane HH mass, d is the interdot distance, S is the overlap between the left and right dot states, $\gamma = (1-\sqrt{1-S^2})/S$, and λ_R is the effective cubic Rashba coefficient with units $[\lambda_R] = \text{energy/momentum}^3$. We neglect the effect of excited orbitals and orbital magnetic contributions which are expected to be valid simplifications at the confinement energies and low magnetic fields considered in this paper. Following Ref. [S7], we express the spin-flip tunneling element in terms of the spin-conserving tunneling element,

$$t_{SO} = \frac{4t_C}{3}\frac{d}{l_{SO}}, \tag{S17}$$

and use this expression as a working definition of the spin-orbit length,

$$l_{SO} = \frac{1}{\lambda_R}\frac{\gamma}{S-\gamma}\frac{4\hbar\omega_0 + d^2 m\omega_0^2}{d^2 m^3\omega_0^3} = \frac{1}{\lambda_R}\frac{1}{\sqrt{1-S^2}}\frac{4\hbar\omega_0 + d^2 m\omega_0^2}{d^2 m^3\omega_0^3}. \tag{S18}$$

Ref. [S7] considers a DQD with a linear SOI, and we find that the spin-orbit length is rather different for systems with a cubic Rashba SOI. In particular, it depends not only on material parameters via λ_R but also on the dot geometry via ω_0, d, S and γ.

This dependence on the dot geometry can be understood from the definition of the spin-orbit length as the distance travelled by a particle before its spin is flipped. Assume for simplicity a particle travelling along x (e.g. the DQD axis) and an nth order Rashba type SOI of the form

$$H_{SO} = \alpha_n(\hbar k_x)^n \sigma_y, \tag{S19}$$

where the real number α_n is the coupling strength with units energy/momentum^n, k_x the crystal momentum along x and σ_y a Pauli matrix. We may then work with an effective spin Hamiltonian by averaging over the crystal momentum,

$$\langle H_{SO}\rangle_\psi = \alpha_n \hbar^n \langle k_x^n\rangle_\psi \sigma_y, \tag{S20}$$

where the state ψ is only required to satisfy the condition $\langle k_x^n\rangle_\psi \neq 0$ to allow for finite spin flip times. In this case the time evolution generated by this Hamiltonian in spin space will cause a spin flip in time $\tau = \pi/(2\alpha_n\hbar^{n-1}\langle k_x^n\rangle_\psi)$. The spin-orbit length along x is then defined to be

$$l_{SO} := \frac{\langle p_x\rangle_\psi}{m}\tau = \frac{\hbar\langle k_x\rangle_\psi}{m}\tau = \frac{\pi}{2}\frac{\hbar^{2-n}}{m\alpha_n}\frac{\langle k_x\rangle_\psi}{\langle k_x^n\rangle_\psi}. \tag{S21}$$

For $n = 1$, the final fraction equals one and the spin-orbit length is a well defined quantity which only depends on material parameters. However, for $n > 1$ the expectation values must be evaluated given a specific state of the system. This introduces two problems: Firstly, since the state must be chosen by hand there is a degree of arbitrariness in the definition of the spin-orbit length. Secondly, given a specific setup, the state chosen for computing the expectation value will depend on the system geometry, and hence the spin-orbit length loses its character as a geometry independent quantity as was explicitly shown above for the case of the cubic ($n = 3$) Rashba SOI. It is therefore necessary to treat the spin-orbit length with caution for nonlinear SOI as it can possibly no longer be considered a good figure of merit for material comparison.

VIII. EFFECT OF THE DOT GEOMETRY ON THE g-FACTORS

Heavy-hole (HH) and light-hole (LH) states confined in a germanium heterostructure in the presence of a magnetic field $\mathbf{B}$ are well described by the Hamiltonian

$$H = \frac{\hbar^2}{2m_0}\left[\left(\gamma_1 + \frac{5}{2}\gamma_s\right)\mathbf{k}^2 - 2\gamma_s\left(\mathbf{k}\cdot\mathbf{J}\right)^2\right] + 2\mu_B\left(\kappa\mathbf{B}\cdot\mathbf{J} + q\sum_{n=1}^{3}B_n J_n^3\right) + V(z) + U(x,y). \tag{S22}$$

Here, the first term is the Luttinger-Kohn Hamiltonian in spherical approximation featuring the Luttinger parameters γ_1 and γ_s, the bare electron mass m_0 and the spin 3/2 matrices J_n. The second term describes the effect of a magnetic field in the context of the envelope function approximation, κ and q being constants that depend on system specific influences such as strain and material composition [S8–S10]. We model the heterostructure by an infinite hard wall potential $V(z)$ in the out-of-plane direction, and realize the quantum dot in the x-y-plane by an elliptical harmonic confinement potential,

$$U(x,y) = \frac{m}{2}\left(\omega_x^2 x^2 + \omega_y^2 y^2\right). \tag{S23}$$

Note that the confinement energies ω_x and ω_y are defined with respect to the in-plane HH mass $m = m_0/(\gamma_1+\gamma_s)$. In the following we assume small magnetic fields in the mT range and neglect orbtial effects arising from the canonical momentum. This is valid for in-plane fields $B_{x,y}$ if $\epsilon_\parallel = \hbar e B_{x,y}/2m \ll \Delta = 2\gamma_s\hbar^2\pi^2/m_0 d^2$, where Δ is the HH-LH splitting with the quantum well width d. At $d \approx 20$ nm one finds $\Delta \approx 17$ meV and hence $\epsilon_\parallel \ll \Delta$ for $B_{x,y} \lesssim 1$ T. On the other hand, for out-of-plane fields B_z we require $\epsilon_\perp = \hbar e B_z/2m \ll \min\{\hbar\omega_x, \hbar\omega_y\}$. For a typical minimal in-plane confinement energy $\min\{\hbar\omega_x, \hbar\omega_y\} \approx 0.5$ meV, we have $\epsilon_\perp/\min\{\hbar\omega_x, \hbar\omega_y\} < 0.05$ at $B_z = 20$ mT which is the maximal field applied in this work.

The eigenstates of the Hamiltonian (S22) in the absence of HH-LH mixing and at zero in-plane magnetic field have the form $|\Psi_h\rangle|j_z\rangle$ ($|\Psi_l\rangle|j_z\rangle$) for $j_z = \pm 3/2$ ($j_z = \pm 1/2$), where j_z is the magnetic quantum number of the total angular momentum, and the position states $|\Psi_{h/l}\rangle$ are a product of simple harmonic oscillator states in x and y and trigonometric functions satisfying the boundary conditions set by $V(z)$ at $\pm d/2$. We proceed to project the Hamiltonian (S22) onto the space spanned by the orthonormal orbital ground state basis $\{|\Psi_h^0\rangle|3/2\rangle, |\Psi_l^0\rangle|1/2\rangle, |\Psi_l^0\rangle|-1/2\rangle, |\Psi_h^0\rangle|-3/2\rangle\}$ with

$$\begin{aligned}
&\Psi_{h/l}^0(x,y,z) = \psi_{h/l}(x,y)\phi(z),\\
&\psi_{h/l}(x,y) = \sqrt{\frac{m_{h/l}\sqrt{\omega_x\omega_y}}{\hbar\pi}}\exp\left(-\frac{m_{h/l}}{2\hbar}\left[\omega_x x^2 + \omega_y y^2\right]\right), \quad \phi(z) = \sqrt{\frac{2}{d}}\cos\left(\frac{\pi z}{d}\right)\Theta\left(\frac{d}{2} - |z|\right),
\end{aligned} \tag{S24}$$

where Θ is the Heaviside step function, $m_h = m$ and $m_l = \sqrt{Mm}$ with in-plane LH mass $M = m_0/(\gamma_1 - \gamma_s)$. Note that $m < M$ for in-plane motion. One obtains a 4×4 matrix (labelled by angular momentum) in which the HH and LH spaces are separated in energy by the HH-LH splitting Δ and can mix due to the intrinsic SOI,

$$\langle H \rangle = \begin{pmatrix} \left(3\kappa + \frac{27}{4}q\right)\mu_B B_z & \sqrt{3}\left(\kappa + \frac{7}{4}q\right)\mu_1\mu_B b^* & -\sqrt{3}\gamma_s\mu_2\hbar(\omega_x - \omega_y) & \frac{3}{2}q\mu_B b \\ \sqrt{3}\left(\kappa + \frac{7}{4}q\right)\mu_1\mu_B b & \epsilon + \left(\kappa + \frac{1}{4}q\right)\mu_B B_z & (5q + 2\kappa)\mu_B b^* & -\sqrt{3}\gamma_s\mu_2\hbar(\omega_x - \omega_y) \\ -\sqrt{3}\gamma_s\mu_2\hbar(\omega_x - \omega_y) & (5q + 2\kappa)\mu_B b & \epsilon - \left(\kappa + \frac{1}{4}q\right)\mu_B B_z & \sqrt{3}\left(\kappa + \frac{7}{4}q\right)\mu_1\mu_B b^* \\ \frac{3}{2}q\mu_B b^* & -\sqrt{3}\gamma_s\mu_2\hbar(\omega_x - \omega_y) & \sqrt{3}\left(\kappa + \frac{7}{4}q\right)\mu_1\mu_B b & -\left(3\kappa + \frac{27}{4}q\right)\mu_B B_z \end{pmatrix}, \tag{S25}$$

where we introduce the quantities

$$b = B_x + iB_y, \quad \epsilon = \frac{\hbar(\omega_x + \omega_y)}{2}\left(\sqrt{\frac{m}{M}} - 1\right) + \Delta, \quad \mu_1 = \langle \psi_h | \psi_l \rangle = \frac{2(mM)^{1/4}}{\sqrt{m} + \sqrt{M}}, \quad \mu_2 = \frac{m^{3/2}(mM)^{3/4}}{m_0(m + \sqrt{mM})^2}. \tag{S26}$$

Note that any additional part of the Hamiltonian that is linear in the momentum (e.g. a Rashba type SOI) vanishes upon projection onto the space spanned by the symmetric ground state wave functions. Assuming the HH-LH splitting to be the largest relevant energy scale, $\Delta \gg \mu_B|\mathbf{B}|, \hbar\omega_x, \hbar\omega_y$, we may perform a Schrieffer-Wolff transformation to decouple the LH subspace. We find an effective 2×2 HH Hamiltonian with a Zeeman term (i.e., a term linear in $\mathbf{B}$) containing the renormalized g-factors

$$g_x = g_x^0 - \xi_1 \frac{\hbar(\omega_x - \omega_y)}{\hbar(\omega_x + \omega_y) - \xi_2\Delta}, \tag{S27a}$$

$$g_y = g_y^0 + \xi_1 \frac{\hbar(\omega_x - \omega_y)}{\hbar(\omega_x + \omega_y) - \xi_2\Delta}, \tag{S27b}$$

$$g_z = g_z^0 - \xi_1 \left[\frac{\hbar(\omega_x - \omega_y)}{\hbar(\omega_x + \omega_y) - \xi_2\Delta}\right]^2, \tag{S27c}$$

where $g_x^0 = g_y^0 = 3q$, $g_z^0 = 6\kappa + 27q/2$ are the effective zeroth order values and

$$\xi_1 = (12\kappa + 21q)\frac{\sqrt{\gamma_1^2 - \gamma_s^2}}{\gamma_1 + \sqrt{\gamma_1^2 - \gamma_s^2}}, \quad \xi_2 = \frac{2\sqrt{\gamma_1 + \gamma_s}}{\sqrt{\gamma_1 + \gamma_s} - \sqrt{\gamma_1 - \gamma_s}} \tag{S28}$$

are material specific constants, $\xi_1 \approx 20.3$ and $\xi_2 \approx 6.0$ in (bulk) germanium. While g_z is always reduced by the HH-LH mixing, the sign of the correction to g_x and g_y depends on the relative in-plane confinement strength. In particular, $g_x \neq g_y$ due to the broken in-plane symmetry. It is therefore possible that one in-plane g-factor becomes negative. This effect can be observed even in a perturbative approach because the zeroth order in-plane g-factors in germanium are small, $g_x^0 = g_y^0 = 3q \approx 0.2$. In contrast, we find that the correction to the out-of-plane g-factor is $|\delta g_z| \lesssim 10^{-2}$ for the values considered here and hence negligible. The smallness of the correction to the out-of-plane g-factor compared to the correction to the in-plane g-factors can be understood as follows: The HH and LH subspaces are mixed by the effect of elliptical confinement ($\sim [\omega_x - \omega_y]$) and the in-plane magnetic fields, and the corrections to the matrix elements in the effective HH Hamiltonian are given by a product of these effects. The effective in-plane g-factor corrections then effectively contain only one of the two small mixing terms ($\delta g_{x,y} \sim [\omega_x - \omega_y]$) because one factor contains the in-plane magnetic field, while the out-of-plane g-factor correction contains two small factors ($\delta g_z \sim [\omega_x - \omega_y]^2$).

IX. ELECTROSTATIC SIMULATION OF THE QUANTUM DOT SHAPES

The hole density is calculated by adapting an electrostatic model of a GaAs device [S11] to the geometry of the SiGe device considered in this work. The electrostatic potential in the plane of the 2D hole gas induced by the gate electrodes is the sum of the potential from each gate weighted by its voltage. The resulting hole density, calculated using the Thomas-Fermi approximation in 2D, contributes to the total electrostatic potential; so an iterative self-consistent solution is computed. We consider a spatially uniform potential offset, which is fitted such that the model produces the experimental hole density when all gate voltages are set to 0V. The value of this potential offset is $-0.307\,\mathrm{V}$. The double quantum dot considered in the experiment has an occupation of (3,2n+1), i.e. 3 holes in the left dot and an unknown number of holes in the right dot. The gate voltages which form these quantum dots are used in the model to produce an occupation of (3,4), taking the floor value of the total charge on each dot. A small

adjustment to the gate voltage strength is required to match the occupation of the left dot which is known from experiment (a global scale factor of 0.955 is applied). The error in the right dot occupation could be explained by the lever arm of the right plunger being 20% lower than that of the left plunger, suggesting that different scale factors for the plunger gates may be appropriate. Such scale factors are beyond the scope of this work, which aims to highlight the different shapes of the two quantum dots.

[S1] G. Granger, G. C. Aers, S. A. Studenikin, A. Kam, P. Zawadzki, Z. R. Wasilewski, and A. S. Sachrajda, Physical Review B **91**, 115309 (2015).

[S2] L. A. Orona, J. M. Nichol, S. P. Harvey, C. G. L. Bøttcher, S. Fallahi, G. C. Gardner, M. J. Manfra, and A. Yacoby, Physical Review B **98**, 125404 (2018).

[S3] P. M. Mutter and G. Burkard, Physical Review Research **3**, 013194 (2021).

[S4] J. Danon and Y. V. Nazarov, Physical Review B **80**, 041301(R) (2009).

[S5] V. N. Golovach, A. Khaetskii, and D. Loss, Physical Review Letters **93**, 016601 (2004).

[S6] P. M. Mutter and G. Burkard, Physical Review B **103**, 245412 (2021).

[S7] D. Stepanenko, M. Rudner, B. I. Halperin, and D. Loss, Physical Review B **85**, 075416 (2012).

[S8] X. Marie, T. Amand, P. L. Jeune, M. Paillard, P. Renucci, L. E. Golub, V. D. Dymnikov, and E. L. Ivchenko, Physical Review B **60**, 5811 (1999).

[S9] R. Winkler, *Spin—Orbit Coupling Effects in Two-Dimensional Electron and Hole Systems* (Springer Berlin Heidelberg, 2003).

[S10] A. V. Trifonov, I. A. Akimov, L. E. Golub, E. L. Ivchenko, I. A. Yugova, A. N. Kosarev, S. E. Scholz, C. Sgroi, A. Ludwig, A. D. Wieck, D. R. Yakovlev, and M. Bayer, ArXiv (2021), 2103.13653.

[S11] D. L. Craig, H. Moon, F. Fedele, D. T. Lennon, B. V. Straaten, F. Vigneau, L. C. Camenzind, D. M. Zumbühl, G. A. D. Briggs, M. A. Osborne, D. Sejdinovic, and N. Ares, ArXiv (2021), 2111.11285.